Electrochemical Optimization and Small-signal Analysis of Grid-connected Polymer Electrolyte Membrane (PEM) Fuel Cells for Renewable Energy Integration

Faegheh Moazeni[a,*] and Javad Khazaei[b]

[a] *Civil & Environmental Engineering Department, School of Science Engineering and Technology, Penn State Harrisburg, 777 W Harrisburg Pike, Middletown, PA 17057. USA.*
fxm53@psu.edu
[b] *Electrical Engineering Department at Penn State Harrisburg (777 W Harrisburg Pike, Middletown, PA 17057. USA), and Architectural Engineering Department at Penn State University Park (State College, PA 16801). USA.*
jxk792@psu.edu

Abstract

In this paper, a small-signal model of a single cell Polymer Electrolyte Membrane Fuel Cell (PEMFC) was developed based on state-space approach to study the effect of various operating conditions on the dynamic responses of the fuel cell. Dynamics of hydrogen, oxygen, and water partial pressure were considered in the modeling procedure. The transient responses of a single- and multiple cell PEMFC were also investigated as the operating parameters of air flow rate, fuel flow rate, temperature, anode/cathode relative humidity level, and electrical current were varied. Next, the studied PEMFC was integrated to the main grid using a boost DC/DC converter and a DC/AC converter. The stability of the overall system was tested through eigenvalue analysis in MATLAB, and several case studies were designed to examine the sensitivity of boost converter parameters and phase-locked loop (PLL) on the stability of the overall system. The analysis results were then validated on a 100 Watt simulated PEMFC in MATLAB Simscape Power System toolbox, and a set of optimum operating conditions were proposed.

Keywords: Small-signal analysis, State-space modeling, Phase-locked loop (PLL), Time-domain simulations, Polymer Electrolyte Membrane Fuel Cell (PEMFC).

1. Introduction

1.1. Problem Statement

The high energy efficiency and considerably low emission of fuel cells have made them potential candidates for energy storage in the past few years [1]. It was in 1970s, after the successful exploitation of fuel cells in the space program that a global interest in fuel cells initiated vast research efforts in this

☆Corresponding author at School of Science Engineering and Technology, Penn State Harrisburg, 777 W Harrisburg Pike, Middletown, PA 17057, Phone: (01)717-948-6111. E-mail: fxm53@psu.edu.

topic. Various forms of fuel cells have been designed that are recognized based on their electrolytes. Some of these include Proton Exchange / Polymer Electrolyte Membrane Fuel Cells (PEMFC), Solid Oxide Fuel Cells (SOFC), Phosphoric Acid Fuel Cells (PAFC), Molten Carbonate Fuel Cells (MCFC), Alkaline Fuel Cells (AFC), Direct Methanol Fuel Cells (DMFC), and Zinc Air Fuel Cells (ZAFC) [2–5]. Although the notion of fuel cell was introduced more than half a century ago and the chemical and physical concepts of it are established, some of its operational difficulties have prevented fuel cells to completely replace conventional batteries. Some of the main challenges include the need for sustainable fuel (i.e. hydrogen in the case of PEMFCs) that is portable and can be safely stored; slow transient response to load changes; and finally the cost. To address the two latter, the control, the design, and the optimum operation of fuel cells should be studied to understand the dynamic behaviour of them as a function of voltage, power, current, and load change. Such is specifically crucial for the fuel cell usage in power systems and electrical vehicles (the two main applications of energy storage) [6, 7].

1.2. Literature Review

There has been a significant effort on modeling and analyzing fuel cells for improved performance and reduced cost [8–18]. To study the effect of water diffusivity, surface roughness, and water content driving force in PEMFCs, the water mass balance and hydration of a PEM fuel cell were formulated by a mathematical zero-dimensional model [8] . The performance of a PEMFC in terms of the operating pressure and voltage was studied, and the efficiency and exergy of the fuel cell was discussed as the voltage, pressure and cleaning process varied in [12]. The effect of flooding on the performance of PEMFCs was studied by developing one-dimensional steady-state model based on a capillary pressure-saturation relationship in [13]. In a separate study, a one-dimensional numerical model was developed to investigate the performance of a PEMFC against operating conditions [14]. A high temperature operating PEMFC with phosphoric acid-doped polybenzimidazole (PBI) membrane was modeled, for which the simulation results showed variable durability of the system with the current density and the membrane doping level. In another study, the performance of a high temperature operating PEMFC under various working conditions was investigated by developing a numerical method with AspenPlus$^{\text{TM}}$ code, a more complex and expensive software compared to MATLAB [15]. A different study proposed a mathematical model able to capture the variations of the gas composition in the anode channel in a dead-ended anode mode operating PEMFC [18]. All the above mentioned references only considered the steady-state operating modes of the PEM fuel cells and ignored the small-signal dynamics.

The dynamic (transient) models investigate step changes in potential and associated circumstances such as gas flow rates, water generation, and current density. Therefore, in a single-cell fuel cell, the transient models reveal how various load requirements are handled. Fuel cells have transient responses that are much slower than the dynamic responses of the typical power conditioner and load to which they are attached. As such, the fuel cell's inability to change its electrical output (current) as quickly as the electrical load changes has significant implications on the overall power system design. Therefore, to design a more efficient fuel cell system, dynamic models are crucial to analyze the performance of fuel cells in a wide range of operating point conditions. Small-signal modeling and analysis is an appropriate dynamic modeling technique to asses the dynamic stability of fuel cell systems for the most efficient response [19]. A few papers studied the small-signal modeling of PEM fuel cells. A small-signal state-space model was developed, and a dynamic model was simulated for a PEMFC in [20], which ignored the fuel cell's electrochemical reactions and AC dynamics. One study developed a state- and transfer function model for a PEMFC coupled with a DC/DC converter [21], yet again, it focused only on the electrical aspects of the fuel cell and the chemical reactions and the operating parameters were not considered.

Another study developed the state-space and thermodynamic models and airflow control for a PEMFC, and used experimental results via LabView to verify the analysis [22]. Nevertheless, the study concentrated mainly on the air excess ratio responses and real-time control of the fuel cell system. In another study, a three-phase converter was designed for PEMFCs in electrical vehicle applications and a circuit model of the converter was developed to control the output voltage [23]. However, the electrochemical or thermodynamic models of the fuel cell and the effects of operating conditions on the output voltage were not discussed. A state-space model of a PEMFC was developed to improve the original state-space model developed by the Department of Energy (DoE) [24]. Although the developed model showed some improvements in transient responses compared to the original DoE model, the focus was on the model validation and not on the small-signal analysis of PEM fuel cells operating in various operating conditions. There exist some studies that discussed modeling and analyzing the stability of PEM fuel cells in smart grids [25–28]. For example, small-signal and large-signal models of the static and dynamic behavior of a PEMFC were developed [26]. However, like in [24], grid integration of the fuel cell was not included. A PEMFC with a boost DC/DC converter was modeled in [28] and the converter control was designed to accomplish the highest efficiency. However, no inverter was included in the study for grid connection. In a more recent study, a fuzzy logic controller was used to test the integration of PEMFCs to the grid [29]. But, it did not discuss the small-signal analysis of the system nor the dynamics of the fuel cell. Overall, the current research in PEM fuel cell stability analysis overlooked either the chemical dynamics (fuel cell stack dynamics) or the electrical dynamics (dynamics of the boost converter and the inverter).

Therefore, to the authors' best of knowledge, the existing literature lacks a comprehensive analysis of PEM fuel cells that not only considers the electrochemical and thermodynamic models of the fuel cell but also takes into account the full grid-connected electrical dynamics of the system considering the performance of the fuel cell under various operating conditions for the maximum efficiency.

1.3. Our Contributions

To address the above limitations in the available research on PEMFCs, this work presents a detailed state-space small-signal model of the PEMFCs for optimizing the performance under different operating conditions, as well as stability analysis for grid-connected PEMFCs. The small-signal and the stability analysis results are then validated using a detailed time-domain simulation model in several scenarios. A summary of our contributions is highlighted as:

- A detailed mathematical analysis considering electrochemical and thermodynamic models associated with the fuel cell stack was developed.
- State-space model of a PEM fuel cell stack was derived considering the fuel cell dynamics, dynamics of the DC/DC boost converter, dynamics of the three-phase inverter, AC dynamics, controller dynamics of the boost converter, and phase-locked loop.
- Eigenvalue analysis was performed to examine the stability of the integrated PEMFCs for grid connections.
- Sensitivity analysis was conducted to investigate potential instability problems associated with DC/DC converter design or inverter parameters.
- Dynamic behavior of the output voltage, also called "voltage" for brevity, was studied as a function of the operating conditions such as number of cells, airflow rate, fuel flow rate, temperature, and current.
- A detailed time-domain simulation model was used to validate and verify the thermodynamic analysis results.
- Case studies were provided to demonstrate the effect of various working parameters on the fuel cell's performance.
- Recommendations were made to optimize the performance of the PEMFC.

1.4. Paper's Outline

The paper's organization is provided in the following: Section 2 describes the system and its small-signal state-space modeling, Section 3 discusses the fuel cell dynamics including all the electrodynamics, electrochemical, and electrical sectors of the PEMFCs, Section 4 discusses stability analysis results, Section 5 includes detailed simulation model and six case studies to verify the analysis results using the time-domain simulations with a discussion subsection to summarize these results, and Section 6 concludes the paper.

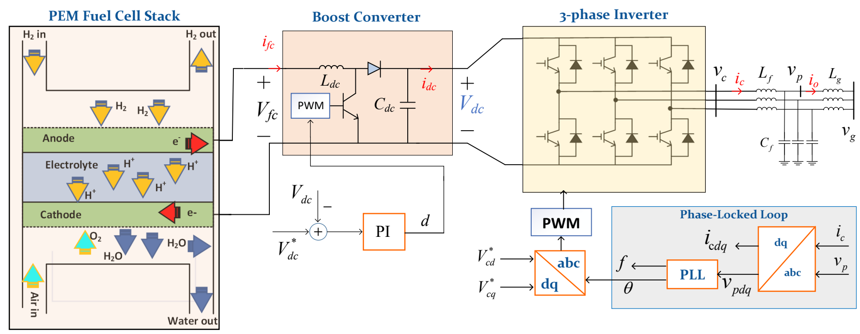

Figure 1: A schematic of a grid-connected PEM fuel cell stack through a boost converter and a three-phase inverter.

2. Small-Signal State-Space Modeling

2.1. System Description and Control

The structure of the studied system is shown in Figure 1. The fuel cell stack provides a low-voltage DC output. In order to connect the fuel cell stack to the grid, which operates in AC mode, an inverter is required to convert the fuel cell's generated DC power to usable AC power. The grid voltage ($v_g(t)$) is represented as a three-phase balanced signal represented by [30]:

$$v_g(t) = \begin{cases} v_{ga}(t) = V_{rms}\sqrt{2}\cos(\omega t) \\ v_{gb}(t) = V_{rms}\sqrt{2}\cos(\omega t - 2\pi/3) \\ v_{gc}(t) = V_{rms}\sqrt{2}\cos(\omega t + 2\pi/3) \end{cases} \tag{1}$$

The inverter is a three-phase voltage source converter (VSC), which has a regulated DC voltage on the DC side and uses two transistors on each phase that switch on/off at high frequency to generate an AC voltage in the output. The process of switching transistors is done by pulse width modulation (PWM) technique.

2.2. Pulse Width Modulation (PWM)

Sinusoidal PWM (SPWM) is normally used in three-phase inverter applications, that uses a sinusoidal reference signal with amplitude V_{ctr} and frequency of $f_n = 60$ Hz to regulate the output voltage of the converter. The sinusoidal reference is compared with a high frequency triangular or a sawtooth waveform to identify switching on each phase of the inverter. This method is represented in Figure 2, where switch operation for upper and lower transistors in each phase is represented by:

$$\begin{cases} V_{ctr} > V_{tri} & \text{Upper Switch is On} \\ V_{ctr} < V_{tri} & \text{Lower Switch is On} \end{cases} \tag{2}$$

In Figure 2, the top figure is the reference sinusoidal waveform, the second plot is the sawtooth waveform at high frequency, and the last two figures are the switching signals for the upper and lower switches in each phase. For switching

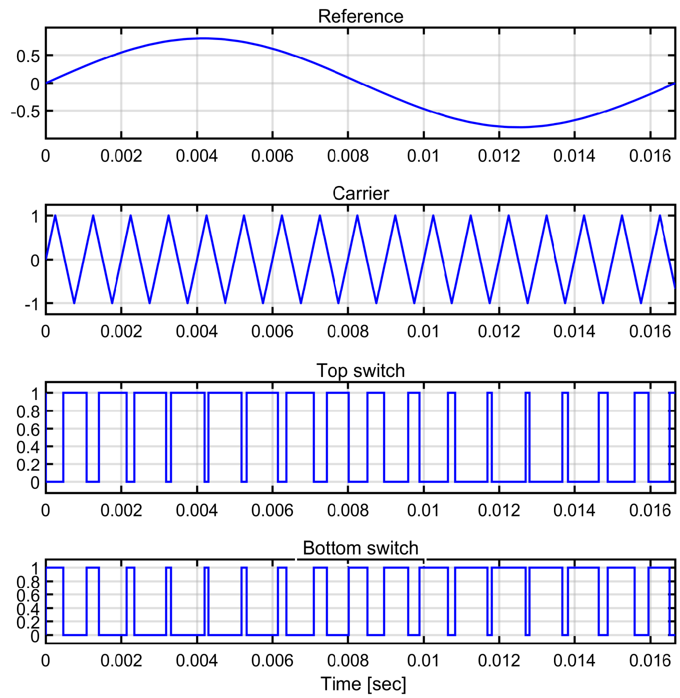

Figure 2: Representation of the SPWM concept for one phase of the inverter.

signals of the other two phases of the inverter, the control signals for phases b and c will be displaced by 120 degrees compared to phase a [31].
Since the output of the converter will be highly distorted (due to high switching frequency of transistors), a passive filter composed of inductive, capacitive, and resistive elements (also known as RLC filter), will be used to mitigate the unwanted harmonics in the output of the converter and generate a pure sinusoidal waveform in the output [32].

2.3. Phase-Locked Loop (PLL), Current, and Power Controllers

On top of the PWM and filter, the inverter should regulate the amount of active and reactive power that is sent to the grid using a closed-loop control. This control mode is also called "grid-connected" mode of operation, where the voltage and frequency is regulated by the grid and the converter only exchanges power with the grid. The converter needs to synchronize itself to the grid, this synchronization is done through a phase-locked loop (PLL) controller that measures the voltage at the point of common coupling (PCC) (point p in Figure 1). The grid-connected operation of the inverter is normally done by vector control in dq reference frame, also known as synchronous reference frame, where proportional integral (PI) regulators can be used to regulate the converter's active and reactive powers. Therefore, the reference signals to be sent to the PWM unit will be derived by transformation of reference voltages in dq frame (V_{cd}^* and V_{cq}^* in Figure 1). The inner current control and active and reactive power controllers will generate the reference voltages in dq frame, V_{cd}^* and V_{cq}^*. The structure of these two control loops is illustrated in Figure 3. The current

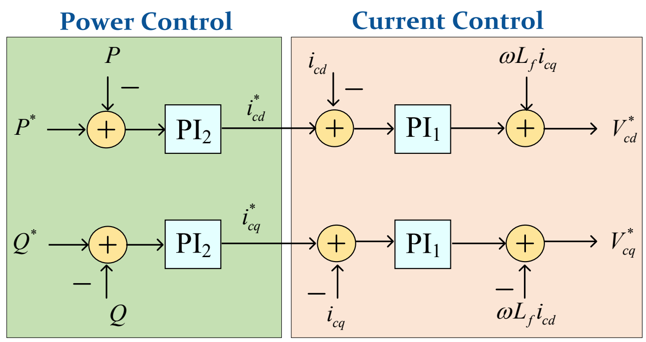

Figure 3: Inverter control in dq frame.

controller is in charge of regulating the converter current in case of faults or failures. When faults occur, high currents will flow into power system components, which might damage the inverter. Therefore, the current controller protects the converter against overcurrents. The input of the inner current controller is the reference dq frame currents, which will be supplemented by the power controller. The reference signals will be compared to the measured converter current in the output, i_{cd} and i_{cq} (which are derived by converting i_c to dq frame using abc to dq conversion block in Figure 1). Decoupling terms are also added to have independent control and active and reactive components of the current. The power controller uses two PI controllers to regulate the error between the measured active/reactive power and the reference values. This controller is called a "vector control", which is widely used in power electronics applications. The readers are encouraged to refer to [32] for more information on vector control of inverters in smart grids.

2.4. DC/DC Boost Converter

For balanced operation, the output voltage of the inverter should have the same magnitude as the grid voltage. For the inverter to generate V_{rms} in the output ($V_c(t)$), the DC side voltage should at least be twice the root mean square (RMS) voltage at the AC side [31]. Therefore, to have an output AC voltage with magnitude of 120 V(AC) in the output of the converter, the DC side voltage should be at least 250 V(DC). However, the PEM fuel cells cannot generate that high DC voltage, therefore, another converter is required in between to boost up the PEM fuel cell's voltage to high voltages around 250 V(DC). A DC/DC boost converter is used to step up the fuel cell's voltage to the level inverter needs (250 V(DC)). Furthermore, this voltage should be regulated so that the inverter generates an AC voltage with fixed magnitude in the output. The voltage regulation is done by controlling the duty cycle of the DC/DC converter switch using a feedback control loop through a proportional integral controller. Details of closed-loop control of DC/DC converters can be found in [32].

2.5. Small-Signal Model of the System

The small-signal model of the overall system will be derived in the following sections. In order to use the state-space modeling technique for the PEM fuel cell, the state variables of the fuel cell need to be represented in first order differential equations [33]. The linearized, small-signal model of the system can then be expressed using equation (3).

$$\Delta\dot{x} = \mathbf{A}\Delta x + \mathbf{B}\Delta u \tag{3}$$

$$\Delta y = \mathbf{C}\Delta x + \mathbf{D}\Delta u \tag{4}$$

where **A** and **B** are system matrices representing the properties of the system and are determined by the fuel cell structure and elements. Matrices **C** and **D** are the output equation matrices that are determined by the particular choice of output variables. In addition, the state variables of the system are represented by the vector Δx, the first order derivatives of the state variables are represented by $\Delta\dot{x}$, the system input vector is Δu, and Δy is the output of the system. In the following, derivation of matrices **A**, **B**, **C**, and **D** for the components of the grid-connected PEM fuel cell is elaborated.

3. PEMFC Dynamics

3.1. Electrochemical Reactions

In polymer electrolyte membrane fuel cells hydrogen is oxidized at the anode and produces H^+ ions and free electrons:

$$H_2 \rightarrow 2H^+ + 2e^- \tag{5}$$

At the cathode, these products will react with oxygen to form water and heat:

$$2H^+ + 2e^- + 0.5O_2 \rightarrow H_2O \tag{6}$$

The two equations of (5) and (6) can be combined as:

$$H_2 + 0.5O_2 \rightarrow H_2O \tag{7}$$

To overcome the slow kinetics of these reactions, the membrane of PEMFCs is coated with highly dispersed catalyst particles, such as platinum or nickel which will reduce the activation energy level and thus expedite the reaction rate. The membrane itself is a material, such as Nafion, made of Perfluorinated Sulfonic Acid (PFSA) which is a synthetic polymer known as polyethylene. Nafion offers great advantages such as durability and hydrophobicity, which will draw the water out of the cell and thus prevent it from flooding [23]. As illustrated in Figure 1, at the anode, the hydrogen ions pass through the proton exchange membrane, moving towards the cathode, while the electrons are transferred out through a wire [34]. At the cathode, the arrived hydrogen ions react with the supplied oxygen and combined with the electrons transported with wire to produce water (Figure 1).

3.2. Voltage Dynamics

While the electrical power and energy output can be calculated from equations (8) and (9), the energy of the chemical inputs and outputs is obtained from the "Gibbs free energy" (ΔG) and Nernst equation (Equations (10) to (12)) [35].

$$p(t) = v(t)i(t) \tag{8}$$

$$e(t) = \int_{t_0}^{t} p(\tau)d\tau \tag{9}$$

where $p(t)$ is the instantaneous output power, $e(t)$ is the energy at anytime, $v(t)$ and $i(t)$ are the time-domain voltage and current, respectively, and t is the time. Consider the reaction (9), then the free Gibbs energy of the total reaction will be [34]:

$$\Delta G = G_{H_2O} - G_{H_2} - 0.5G_{O_2} \tag{10}$$

where G_{H_2O}, G_{H_2}, and G_{O_2} refer to the free Gibbs energy of water, hydrogen, and oxygen, respectively. At the same time,

$$\Delta G = -zFE_{cell} \tag{11}$$

where z is the number of electrons transferred in the redox reactions, F is the Faraday constant (9.64853399×10^4 coulombs per mole of electrons), and E_{cell} is the electrical energy of the cell.

On the other hand, according to the Nernst equation, electrical energy of the cell can be calculated from the activity of the products and reactants as [36]:

$$E_{cell} = \frac{RT}{zF} \times \ln\left(\frac{c_{H_2} \times c_{O_2}^{0.5}}{c_{H_2Oc}}\right) \tag{12}$$

where R is the universal gas constant equal to 8.314 $J/mole.K$, T is the temperature in K, and c_{H_2Oc}, c_{H_2}, and c_{O_2} are the concentrations of water vapour in the cathode, hydrogen, and oxygen gas, respectively. According to the ideal gas law, the concentration of a gas component is equivalent to its partial pressure [34]. Therefore,

$$E_{cell} = \frac{RT}{zF} \times \ln\left(\frac{PH_2 \times PO_2^{0.5}}{PH_2O_c}\right) \tag{13}$$

where PH_2O_c, PH_2, and PO_2 are the partial pressures of water vapour in cathode, hydrogen, and oxygen gas respectively. The cell voltage equation after the circuit is closed will be:

$$V_{cell} = E^{\circ} + E_{cell} - L \tag{14}$$

where E° is the open circuit voltage of the cell and L is the voltage losses. Replacing E_{cell} from equation (9) will result in:

$$V_{cell} = E^{\circ} + \frac{RT}{zF} \times \ln\left(\frac{PH_2 \times PO_2^{0.5}}{PH_2O_c}\right) - L \tag{15}$$

The output voltage for a fuel cell stack containing N cells will be $V_{out} = NV_{cell}$:

$$V_{out} = N(E^{\circ} + \frac{RT}{zF} \times \ln\left(\frac{PH_2 \times PO_2^{0.5}}{PH_2O_c}\right) - L) \tag{16}$$

where V_{out} is the output voltage of the fuel cell stack and N is the number of cells in each stack.

3.3. Voltage Losses; Fuel Cell Irreversibilities

The concomitant voltage losses can be summarized as follows:

1. Activation losses, occurring at the surface of the electrodes and representing the slowness of the reactions. These losses can be calculated from the "Tofel equation" as [23]:

$$\Delta V_{act} = a \times \log(\frac{i}{i_o}) \tag{17}$$

   where a is a constant, i is the current density ($A.cm^{-2}$) and i_o is the "exchange-current density".

2. Internal currents and fuel crossover, caused by passing a small amount of electrons through the electrolyte from the anode to the cathode, instead of being collected at the anode for electricity production. This loss can be calculated from [23]:

$$\Delta V_{act} = -A \times \ln(\frac{i + i_n}{i_o}) \tag{18}$$

$$A = \frac{RT}{2\alpha F}$$

   where i_n is the internal current density and α is the chargetransfer coefficient and is equal to the ratio of the electrical energy applied that is captured in changing the rate of an electrochemical reaction.

3. Ohmic (or resistive) losses, measuring the resistance to the flow of ions through the electrolyte and are directly proportional to the current density. The ohmic losses can be calculated from the Ohm's law [23]:

$$\Delta V = ir \tag{19}$$

where r is the output resistance in kΩ cm^2 and ΔV is voltage gain in volts.

4. Concentration or masstransport losses, stemmed from the concentration variations of the reactants at the surface of the electrodes as the fuel is being consumed. These losses are expressed in terms of a voltage *gain* and calculated as:

$$\Delta V = -\frac{RT}{2F} \times \ln(1 - \frac{i}{i_l}) \tag{20}$$

or simplified as

$$\Delta V = -b \times \ln(1 - \frac{i}{i_l}) \tag{21}$$

where b is a constant and i_l is the limiting current density related to concentration losses.

Combining all four categories of fuel-cell irreversibilities (or losses), L will be defined as:

$$L = (i + i_o)r + a \times \ln(\frac{i + i_n}{i_o}) - b \times \ln(1 - \frac{i + i_o}{i_l}) \tag{22}$$

Replacing L in equation (16) with equation (22), the output voltage of fuel cell considering its losses can be obtained.

3.4. PEMFC Small-signal Model

A key concern in the PEMFCs is the hydration and water movement. While ample water is essential in the electrolyte to keep the proton activity at a high level, the content of the water must be carefully managed to prevent flooding in either of the catalyst layers. Therefore, three state variables of the system would be the flow rates of inlet hydrogen and oxygen, as well as the inlet water vapor flow rate to the cathode. The number of gas molecules in the cell was obtained from the ideal gas law, $PV = nRT$, where P is the partial pressure of the gas (Pa), V is the volume of the anode or the cathode, and n is the number of gas molecules present in the cell, which is equal to the gas molecules in the inflow minus the produced/consumed flow and outflow [23]. For instance, for inlet hydrogen gas, the ideal gas law will be written as $PH_2 . V_A = n_{H_2} R\ T$, where V_A is the anode volume in m^3, and $n_{H_2} = n_{H_2}^{in} - n_{H_2}^{con} - n_{H_2}^{out}$. Differentiating PH_2 with respect to t, the first state equation is derived as:

$$\frac{dPH_2}{dt} = \frac{RT}{V_A} \left(n_{H_2}^{in} - n_{H_2}^{con} - n_{H_2}^{out} \right) \tag{23}$$

Similarly, the state equations for oxygen and water were derived for each gas component, expressed as:

$$\frac{dPO_2}{dt} = \frac{RT}{V_C}\left(n_{O_2}^{in} - n_{O_2}^{con} - n_{O_2}^{out}\right) \tag{24}$$

$$\frac{dPH_2O_C}{dt} = \frac{RT}{V_C}\left(n_{H_2O_C}^{in} - n_{H_2O_C}^{pro} - n_{H_2O_C}^{out}\right) \tag{25}$$

where V_C is the cathode volume in m^3, $n_{H_2}^{con} = 2K_rA_ci$, $n_{O_2}^{con} = K_rA_ci$, $n_{H_2O_c}^{pro} = 2K_rA_ci$, $K_r = \dfrac{N}{4F}$, and

$$n_{H_2}^{out} = \frac{P_{H_2}}{P_A}(F_A^{in} - 2K_rA_ci) \tag{26}$$

$$n_{O_2}^{out} = \frac{P_{O_2}}{P_C}(F_C^{in} - K_rA_ci) \tag{27}$$

$$n_{H_2O_C}^{out} = \frac{P_{H_2O_c}}{P_C}(F_C^{in} + 2K_rA_ci) \tag{28}$$

where A_c is the cell active area (cm^2), $P_A = P_{H_2} + P_{N_2}$, $P_C = P_{N_2} + P_{O_2} + P_{H_2O_C}$, F_A^{in} is the anode inlet flow rate, and F_C^{in} is the cathode inlet flow rate. By replacing (26), (27) and (28) in (23), (24) and (25), the state-space model of the system was derived. By linearizing the system around an operating point, the small-signal model of the system was derived, where $\Delta x_{FC} = [\Delta PH_2, \Delta PO_2, \Delta PH_2O_C]^T$, $\Delta u_{FC} = [\ \Delta n_{H_2}^{in}, \Delta n_{O_2}^{in}, \Delta n_{H_2O_C}^{in}, \Delta i\ ]^T$ and variable with a "Δ" representing the small-signal variations. The operating point of the system is presented in Table 1, and the state matrices of the system are represented in the following:

Table 1: The operating point of the system [10, 23]

Parameter	Value	Unit
$n_{H_2}^{in}$	0.005	$moles.s^{-1}$
$n_{O_2}^{in}$	0.0018	$moles.s^{-1}$
$n_{H_2O_C}^{in}$	0.072	$moles.s^{-1}$
$n_{H_2O_A}^{in}$	0.0029	$moles.s^{-1}$
$n_{N_2}^{in}$	0.0062	$moles.s^{-1}$
T	338.15	K
A_c	136.7	cm^2
V_A	6.495	cm^3
V_C	12.96	cm^3
i	0.073	$A.cm^{-2}$
r_f	30.762	$\mu.\Omega.m^2$
N	1	number

The coefficient matrices of A_{FC}, B_{FC}, C_{FC}, and D_{FC} for the PEMFC were obtained as:

$$A_{FC} = RT \begin{bmatrix} -(F_A^{in} - 2K_rA_ci)\dfrac{P_{H_2O_A}}{V_AP_A^2} & 0 & 0 \\ 0 & -(F_C^{in} - K_rA_ci)\dfrac{P_{N_2}+P_{H_2O_C}}{V_CP_C^2} & -(F_C^{in} - K_rA_ci)\dfrac{P_{O_2}}{V_CP_C^2} \\ 0 & (F_C^{in} + 2K_rA_ci)\dfrac{P_{H_2O_C}}{V_CP_C^2} & -(F_C^{in} + 2K_rA_ci)\dfrac{P_{N_2}+P_{O_2}}{V_CP_C^2} \end{bmatrix}$$

$$B_{FC} = RT \begin{bmatrix} \dfrac{1}{V_A}\left(1 - \dfrac{F_A^{in}P_{H_2}}{n_{H_2}^{in}P_A}\right) & 0 & 0 & -2K_rA_c\dfrac{P_{H_2O_A}}{V_AP_A} \\ 0 & \dfrac{1}{V_C}\left(1 - \dfrac{F_C^{in}P_{O_2}}{n_C^{in}P_C}\right) & \dfrac{-2F_C^{in}P_{O_2}}{V_Cn_C^{in}P_C} & -K_rA_c\dfrac{P_{N_2}+P_{H_2O_C}}{V_cP_C} \\ 0 & \dfrac{-2F_C^{in}P_{H_2O_C}}{V_Cn_C^{in}P_C} & \dfrac{1}{V_C}\left(1 - \dfrac{F_C^{in}P_{H_2O_C}}{n_C^{in}P_C}\right) & 2K_rA_c\dfrac{P_{N_2}+P_{O_2}}{V_cP_C} \end{bmatrix}$$

where $n_C^{in} = (n_{O_2}^{in} + n_{H_2O_C}^{in})$ and C_{FC} and D_{FC} matrices are defined as:

$$C_{FC} = N[\frac{RT}{2FPH_2}, \frac{RT}{4FPO_2}, \frac{-RT}{2FPH_2O_C}],$$

$$D_{FC} = N[0,\ 0,\ 0,\ -r_f]$$

where $r_f = r + \dfrac{a}{i+i_n} + \dfrac{b}{i_l - i - i_n}$.

3.5. Boost Converter Dynamics

The input voltage of the fuel cell is stepped up by a boost converter to produce satisfactory DC-link voltage for the three-phase inverter of PEMFC. A PI control loop is used to regulate the DC-link voltage, which will be modeled in this section. The state-space model of the DC/DC boost converter is exhibited by the state-space averaging technique [37]. According to Figure 1, the boost converter dynamics can be developed as (29) and (30).

$$\frac{di_{fc}}{dt} = \frac{1}{L_{dc}}V_{fc} - \frac{(1-d)}{L_{dc}}V_{dc} \tag{29}$$

$$\frac{dV_{dc}}{dt} = \frac{(1-d)}{C_{dc}}i_{fc} - \frac{1}{C_{dc}}i_{dc} \tag{30}$$

where V_{fc} and i_{fc} are the input DC voltage and current from fuel cell stack, respectively, d is the duty cycle of the boost converter, and V_{dc} and i_{dc} are the output DC voltage and current of the boost converter, respectively. For simplicity, i_{dc} is shown in terms of DC-link voltage and state variables associated with the AC dynamics of the system, where $V_{dc}i_{dc} = \frac{3}{2}(v_{pd}i_{od} + v_{pq}i_{oq})$ is used to eliminate i_{dc} from the small-signal model and represent it in terms of state variables [30]. The above equation is linearized around an operating point and rearranged to represent the the small-signal dynamics of i_{dc}.

$$\hat{i}_{dc} = \frac{3}{2V_{dc0}}\left(v_{pq0}\hat{i}_{oq} + v_{pd0}\hat{i}_{od} + i_{od0}\hat{v}_{pd} + i_{oq0}\hat{v}_{qd}\right) - i_{dc0}\hat{V}_{dc} \tag{31}$$

The overall state space model of the boost converter is acquired if (31) is replaced in boost converter dynamics ((29) and (30)). Referring to Figure 1, dynamics of the DC/DC converter controller can be written as (32).

$$d = (k_{pi} + \frac{k_{ii}}{s})(V_{dc}^{*} - V_{dc}) \tag{32}$$

where k_{pi} and k_{ii} are the proportional and integral gains of the boost converter's PI controller.

3.6. AC Filter Dynamics

As laid out in Figure 1, the AC dynamics incorporate the dynamics of the LCL filter. The AC dynamics of the system is derived by applying Kirchhoff's voltage and current laws (KVL and KCL) in the main AC loops and converting the equations to dq reference frame, shown in equations (33)-(35). Details of synchronous reference frame and converter control can be found in [30].

$$\frac{d}{dt}\begin{bmatrix} i_{cd} \\ i_{cq} \end{bmatrix} = \begin{bmatrix} 0 & \omega \\ -\omega & 0 \end{bmatrix}\begin{bmatrix} i_{cd} \\ i_{cq} \end{bmatrix} - \frac{1}{L_f}\begin{bmatrix} v_{pd} \\ v_{pq} \end{bmatrix} + \frac{V_{dc}}{2L_f}\begin{bmatrix} d_d \\ d_q \end{bmatrix} \tag{33}$$

$$\frac{d}{dt}\begin{bmatrix} i_{od} \\ i_{oq} \end{bmatrix} = \begin{bmatrix} 0 & \omega \\ -\omega & 0 \end{bmatrix}\begin{bmatrix} i_{od} \\ i_{oq} \end{bmatrix} + \frac{1}{L_g}\begin{bmatrix} v_{pd} \\ v_{pq} \end{bmatrix} - \frac{1}{L_g}\begin{bmatrix} v_{gd} \\ v_{gq} \end{bmatrix} \tag{34}$$

$$\frac{d}{dt}\begin{bmatrix} v_{pd} \\ v_{pq} \end{bmatrix} = \begin{bmatrix} 0 & \omega \\ -\omega & 0 \end{bmatrix}\begin{bmatrix} v_{pd} \\ v_{pq} \end{bmatrix} + \frac{1}{C_f}\left(\begin{bmatrix} i_{cd} \\ i_{cq} \end{bmatrix} - \begin{bmatrix} i_{od} \\ i_{oq} \end{bmatrix}\right) \tag{35}$$

where d_d and d_q are the duty cycles of the inverter in dq frame. The converter reference voltages in dq frame (v_{cd}^{*} and v_q^{*}) can also be expressed in terms of duty cycles ($v_{cd}^{*} = 0.5V_{dc}d_d$ and $v_q^{*} = 0.5V_{dc}d_q$). The small-signal model of the AC side is obtained by linearizing (33)-(35) around an operating point, the result is depicted in the state-space form in (36).

$$\dot{x_{ac}} = A_{ac}x_{ac} + B_{ac}u_{ac} \tag{36}$$

where

$$X_{ac} = [\hat{i}_{cd}, \hat{i}_{cq}, \hat{i}_{od}, \hat{i}_{oq}, \hat{v}_{pd}, \hat{v}_{pq}], u_{ac} = [\hat{d}_d, \hat{d}_q, \hat{v}_{gd}, \hat{v}_{gq}, \hat{V}_{dc}, \hat{\omega}]$$

and A_{ac} and B_{ac} were defined in the following:

$$A_{ac} = \begin{bmatrix} 0 & \omega_0 & 0 & 0 & -\frac{1}{L_f} & 0 \\ -\omega_0 & 0 & 0 & 0 & 0 & -\frac{1}{L_f} \\ 0 & 0 & 0 & \omega_0 & \frac{1}{L_g} & 0 \\ 0 & 0 & -\omega_0 & 0 & 0 & \frac{1}{L_g} \\ \frac{1}{C_f} & 0 & -\frac{1}{C_f} & 0 & 0 & -\omega_0 \\ 0 & \frac{1}{C_f} & 0 & -\frac{1}{C_f} & -\omega_0 & 0 \end{bmatrix} \tag{37}$$

$$B_{ac} = \begin{bmatrix} \frac{V_{dc0}}{L_f} & 0 & 0 & 0 & \frac{d_{d0}}{L_f} & i_{cq0} \\ 0 & \frac{V_{dc0}}{L_f} & 0 & 0 & \frac{d_{q0}}{L_f} & -i_{cd0} \\ 0 & 0 & -\frac{1}{L_g} & 0 & 0 & i_{od0} \\ 0 & 0 & 0 & -\frac{1}{L_g} & 0 & -i_{oq0} \\ 0 & 0 & 0 & 0 & 0 & v_{pd0} \\ 0 & 0 & 0 & 0 & 0 & -v_{pq0} \end{bmatrix} \tag{38}$$

3.7. Inverter Control Dynamics

Figure 3 demonstrates the schematic of the fuel cell's three-phase inverter control. As discussed in Section 2.3, the controller is comprised of two cascaded loops of current control and power control. The inner current loop controls the converter output current using two PI loops, whereas the outer loop exclusively regulates the output active and reactive powers of the fuel cell system sent to the grid. As was illustrated earlier in Figure 1, a phase-locked loop (PLL) is also included to synchronize the converter to the grid at the point of common coupling.

3.7.1. Inner Current Controller Dynamics

The inner current control uses PI controllers and feedforward loops to provide the fuel cell's reference dq frame voltages. Dynamics of the inner control are written as:

$$v^*_{cd} = \underbrace{(k_{pi} + \frac{k_{ii}}{s})}_{PI_1(s)}(i^*_{cd} - i_{cd}) - \omega L_f i_{cq} \tag{39}$$

$$v^*_{cq} = \underbrace{(k_{pi} + \frac{k_{ii}}{s})}_{PI_1(s)}(i^*_{cq} - i_{cq}) + \omega L_f i_{cd} \tag{40}$$

where k_{pi}, k_{ii} are the proportional and integral gains of the inner loop's PI controllers and v^*_{cd}, v^*_{cq} are the reference voltages generated by the inner current control loop. In modern power electronics converters, the switching losses are negligible and therefore, the dynamics of the pulse width modulation (PWM) control can be ignored [30]. In this case, the converter tracks the reference voltages very fast and therefore, $v_{cd} \approx v^*_{cd}, v_{cq} \approx v^*_{cq}$.

3.7.2. PLL Dynamics

The PLL uses a PI controller to integrate the converter with the grid by controlling the q component of (v_{pq}) to zero. Dynamics of the PLL can be derived as [38]:

$$\hat{\omega} = -\left(k_p^{pll} + \frac{k_i^{pll}}{s}\right)\hat{v}_{pq} \tag{41}$$

$$\hat{\theta} = \frac{1}{s}\hat{\omega} \tag{42}$$

where k_p^{pll}, k_i^{pll} are the PLL's regulator gains.

3.7.3. Outer Loops Dynamics

The outer power loop generates reference currents for the inner current control loop to regulate the active and reactive powers supplied to the grid. Dynamics of the power controller is given by (43), (44).

$$i_{cd}^* = \underbrace{(k_{pp} + \frac{k_{ip}}{s})}_{PI_2(s)}(P^* - P) \tag{43}$$

$$i_{cq}^* = \underbrace{(k_{pq} + \frac{k_{iq}}{s})}_{PI_2(s)}(Q^* - Q) \tag{44}$$

where k_{pp}, k_{ip} are the active power's PI controller gains and k_{pq}, k_{iq} are the reactive power's PI controller gains. Equations (39)-(23) are then linearized to develop the small-signal model of the three-phase inverter. The obtained active and reactive powers are also linearized around an operating point, where $P = \frac{3}{2}\left(v_{pd}i_{od} + v_{pq}i_{oq}\right)$ and $Q = \frac{3}{2}\left(v_{pq}i_{od} - v_{pd}i_{oq}\right)$.

4. Stability Results

Figure 1 illustrated the derived small-signal model of the proposed control framework and Figure 3 was implemented on different case studies in this section for stability analysis. The fuel cell parameters are adopted from [23]. In reality, the fuel-cell will act as a constant voltage source with slow dynamics and control parameters of the converters provide a much faster response. This can be explained by the fact that the converters are operated at high frequency switching (normally, 100-500 kHz). This means the converters respond to changes in the system in a few microseconds, while the fuel cell responses are in a few seconds. Therefore, the control parameters can be designed and tuned individually. For this research, the individual control loop parameters were designed using simplified closed-loop dynamics. The readers are encouraged to refer to [30, 39, 40] for more information. Parameters of the boost converter and the inverter are shown in Table 2.

4.1. Eigenvalue Results

The state-space linearized model was extracted using the Simulink, at a given operating point. A detailed procedure for the initial conditions calculations were provided in [41]. MATLAB's "LINMOD" function was applied on a developed

Table 2: Parameters of the system

Parameter	Value	Parameter	Value	Parameter	Value
V_{dc}	250 V	V_g	120 $\mathrm{V_{rms}}$	k_{pp}	0.1
L_g	4 mH	f	60 Hz	k_{ip}	1
L_{dc}	1 μH	C_{dc}	1 mF	k_{pq}	0.05
L_f	500 μH	C_f	100 μF	k_{iq}	5
k_{ip}, k_{ii}	2.5, 0.3	k_p^{pll}	100 μF	k_i^{pll}	1800

simulink model to calculate the state-space linearized matrices A, B, C, D of the integrated system. The results were used for eigenvalue analysis. Eigenvalues of the system are shown in Table 2. As demonstrated in Table 3, the system

Table 3: Eigenvalues of the system

Eigenvalue	Frequency, f (Hz)	Damping, ζ (%)
λ_1=$-1.2e^6 + j376.99$	60	100
λ_2=$-1.2e^6 - j376.99$	-60	100
λ_3=$-1.2e^3 + j9085.60$	1446	64
λ_4=$-1.2e^3 - j9085.60$	-1446	64
λ_5=$-1.1e^3 + j8354.76$	1330	64
λ_6=$-1.1e^3 - j8354.76$	-1330	64
λ_7=$-292.1 + j1040.89$	166	87
λ_8=$-292.1 - j1040.89$	-166	87
λ_9=-205.88	0	100
λ_{10}=-53.64	0	100
λ_{11}=-1	0	100
λ_{12}=-0.35	0	100
λ_{13}=-0.12	0	100
λ_{14}=-0.12	0	100
λ_{15}=-0.077	0	100

resulted in 15 eigenvalues, all of which located at the left half-plane and thereby the integrated system is stable. The sensitivity analysis is conducted to investigate the effect of PEMFC parameters on overall stability of the integrated system. It was observed that modifying the fuel cell stack parameters such as temperature, number of cells, and input pressure around an acceptable range, does not have a major impact on the stability of the system and eigenvalues of the system remain on the open left half plane (OLHP). However, by modifying the DC/DC or DC/AC converter parameters, the stability of the system is challenged. This is justified by the fact that dynamics of the fuel cell stack are very slow compared to fast dynamics of power electronics converters. In the following, a sensitivity analysis is conducted to analyze the effect of DC/DC or DC/AC converter parameter change on eigenvalues of the system.

4.2. Effect of L_{dc}

The sensitivity of boost converter inductance (L_{dc}) on stability of the overall system was investigated. A gain K was multiplied by the inductance value. As the gain was increased from 1 to 30, for each of which the eigenvalues were plotted, the impact of the increasing boost converter inductance value on stability of the system was studied through eigenvalue analysis, illustrated in Figure 4. It was shown that as the inductance value was increased, λ_7, λ_8, and λ_9 moved towards the origin, but the system remained stable.

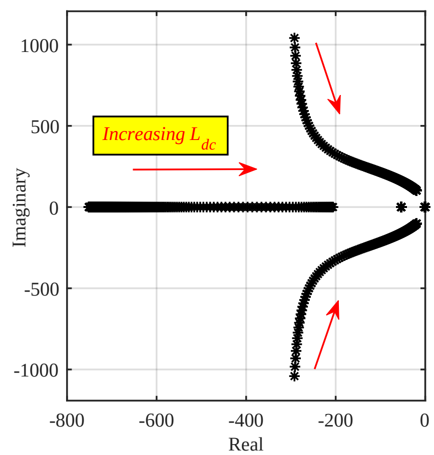

Figure 4: Effect of increasing L_{dc} on stability of the system.

4.3. Effect of C_{dc}

The DC-link capacitor value was multiplied by a gain (K), while the gain value varied from 1 to 100. Figure 5 demonstrated the eigenvalues plot for the sensitivity of an increasing DC-link on stability of the system. As the DC-link capacitor was increased by 100 times, λ_7 and λ_9 advanced to the right half-plane and consequently the system became unstable. This indicated that the system was very sensitive towards increasing the DC-link capacitor value.

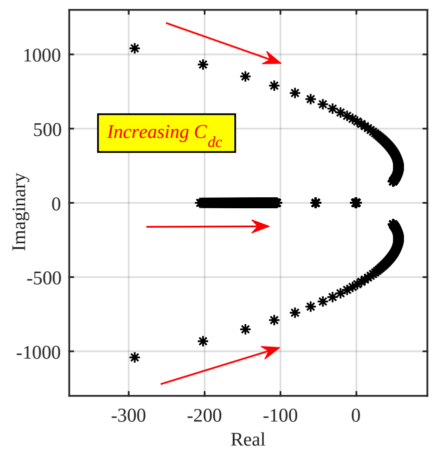

Figure 5: Effect of DC-link capacitor on stability of the system.

4.4. Effect of Boost Converter Controller Gains

The impact of increasing DC/DC converter controller gains on stability of the overall system was explored. The controller gains were multiplied by a gain (K) varying from 1 to 30. Figure 6 exhibited the stability analysis results. As the boost converter controller gains increased by 30 times, the eigenvalues moved to the right half-plane and the system became unstable.

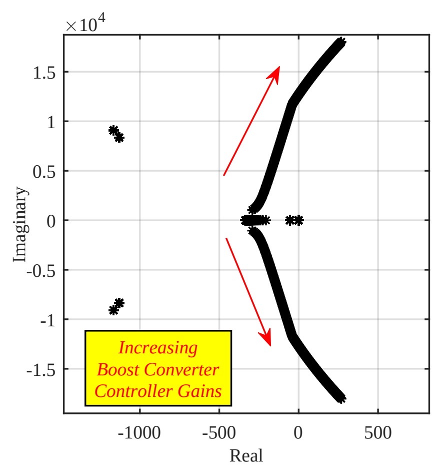

Figure 6: Effect of boost converter controller gains on stability of the system.

4.5. Effect of PLL Gains

The effect of increasing PLL gains from 1 to 30 on the stability of the system was studied. The results shown in Figure 7 indicated the significant role of the

PLL on stability of a grid-connected fuel cell system. As the PLL gains were increased, λ_5 and λ_6 moved to the right half-plane and the system became unstable.

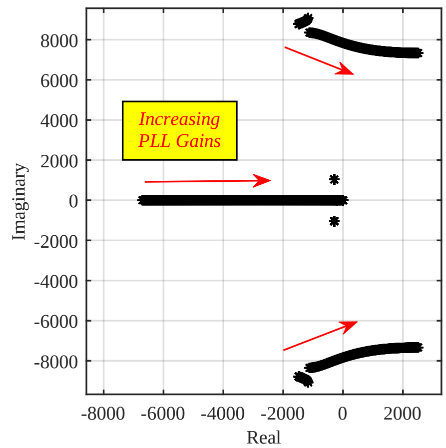

Figure 7: Effect of PLL gains on stability of the system.

5. Electrochemical Optimization of Fuel Cell Stack Case Studies

The developed state-space model was used to optimize the operating parameters of a PEMFC. To validate the state-space results, a detailed time-domain PEM fuel cell model was also simulated using Simscape Power System toolbox of MATLAB and detailed comparisons were carried out. The simulated model included a 100W PEMFC stack connected to a 1.68 Ω resistive load. The parameters of the PEM cell were equal to the state-space model parameters listed in Table 1, unless were not tunable in the Simscape. Six case studies were carried out to analyze the performance of the system.

5.1. Case Studies

5.1.1. Voltage and power versus cell number

The output voltage of the fuel cell versus (vs.) cell number was studied. Results are illustrated in subplots (a) and (b) in Figure 8, where the left subplot shows the time-domain simulations and the right subplot depicts the analysis results. The output voltage decreased as the cell number increased. This was because of the voltage loss across each cell. However, as demonstrated in subplots (c) and (d) in Figure 8, the output power of the fuel cell increased as the cell number increased. Our results showed that the output power generated by a PEMFC with 20 cells was more than 20 times higher than that of a 1-cell PEMFC, while the voltage drop in the 20-cell stack was only 8.4% higher than the loss in a 1-cell stack, emulating equation 22. Due to this voltage drop, the power acquired via simulation was not as high as that obtained from analysis. As shown in Figure 8, the state-space analysis results followed the same pattern as the simulation results.

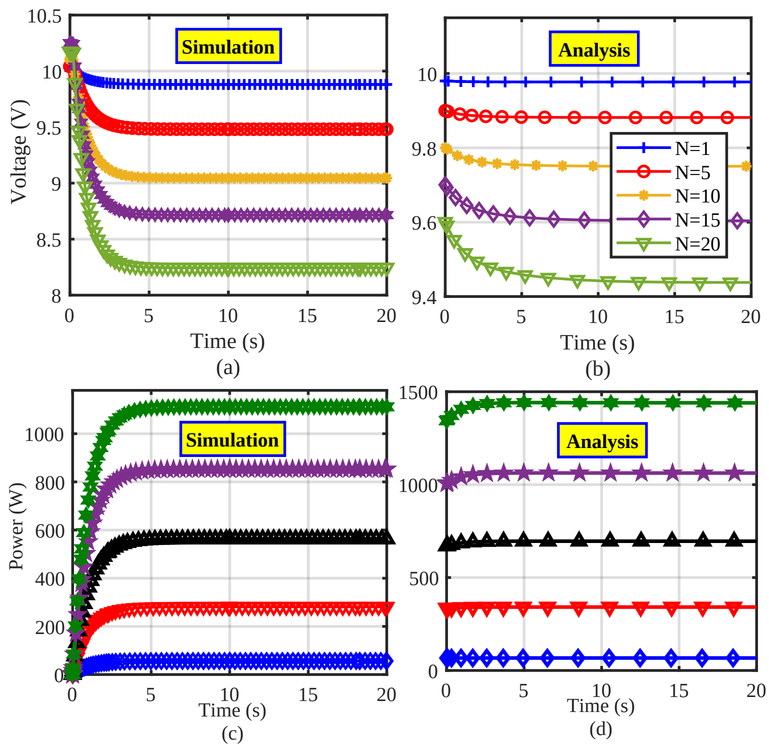

Figure 8: Results for the Voltage and power vs. cell number. Subplots (a) and (b): Output voltage of the PEMFC vs. cell number. Both the simulation (left) and the analysis (right) results showed a voltage drop as the cell number increased. Subplot (c) and (d): Output power of the PEMFC vs. cell number. Both the simulation (left) and the analysis (right) results showed an increase in power as the cell number increased.

5.1.2. Voltage as a function of fuel flow rate

The effect of fuel flow rate on the output voltage of the PEMFC was evaluated. Figure 9 demonstrated an exponential decay in both simulated and analysis results for dynamic behavior of the output voltage, dropping from 10 down to about 9.8V in the first 5 seconds and remained steady after. The analysis results did not show any difference in the outlet voltage when the fuel flow rate was increased from 0.5 to 3.7 liter per minute (Lpm). The simulation results, however, showed slightly different voltage values as the lowest being 9.756V at the lowest amount of fuel (0.5 Lpm) and the highest being 9.882V for the highest fuel flow rate of 3.7 Lpm. Such a small influence of hydrogen flow rate on voltage could be due to the high purity of hydrogen (99.99%) and thus its abundance, much higher than the stoichiometric requirements, even at the lowest flow rate of 0.5 *Lpm*.

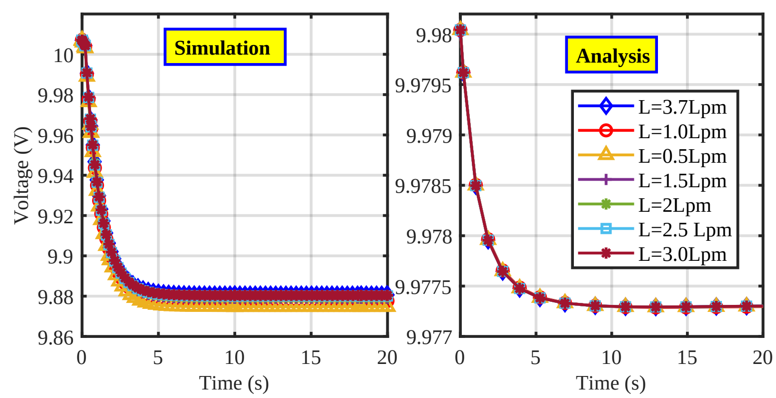

Figure 9: Output voltage (V) of the PEMFC vs. the inlet hydrogen flow rate (*Lpm*).

5.1.3. Voltage as a function of air flow rate

In this case, the air flow rate was modified to evaluate the output voltage performance. The oxygen was supplied at the cathode in the form of air, which had the purity of 21% for oxygen. It was mentioned in Section 3.3 that as the reactant gas is extracted, the concentration of the oxygen in the cathode will slightly decrease which results in a (small) voltage reduction. As demonstrated by Figure 10, a similar pattern was observed for the dynamic behavior of the output voltage in both the simulation and analysis results. Voltage decreased exponentially in the first 5 seconds from 9.98 down to 9.97675V in the analysis and from 10.01 to 9.879V in the simulation models, and then entered a steady-state condition. The difference between the voltage level for the lowest (1*Lpm*) and the highest (20*Lpm*) air flow rates was 2.5mV and 2mV for analysis and simulation models, respectively. The highest voltage in both sets of results was obtained at the highest amount of air (i.e. oxygen) at the cathode, while the lowest voltage associated with to the lowest air flow rates.

5.1.4. Voltage as a function of temperature

This case investigated the effect of temperature on the output voltage of the PEMFC. Temperature was changed in the range of 25 to 65°C, which is the typical operating range in various PEM fuel cell systems. Similar to the previous cases, regardless of the temperature, the output voltage plummeted steeply in the first 5 seconds and then remained constant after. As exhibited in Figure 11, the output voltage obtained from the simulation model of the PEMFC (the left subplot) decreased from 9.898 to 9.88V as T was ranged from 65°C to 25 °C, respectively, whereas the difference in voltage values was not detectable in the state-space modeling (the right subplot) as temperature varied within the same range. The small impact of temperature on the output voltage could be

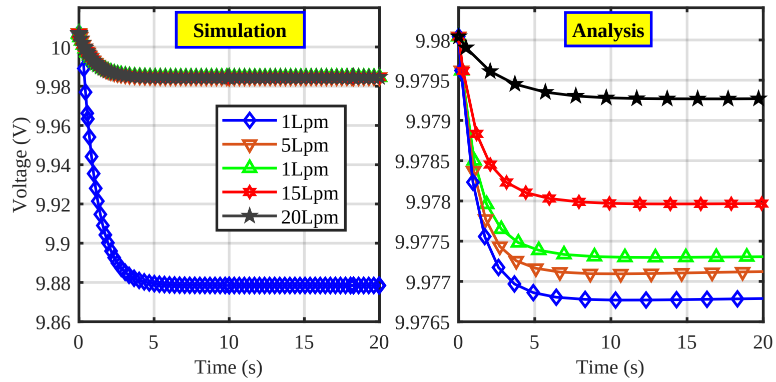

Figure 10: Output voltage (V) of the PEMFC vs. the inlet air flow rate (Lpm).

explained by the relationship between the gas densities and temperature. According to the Charles's Law [42], the density of gases (and thus their mole numbers over a fixed volume) is inversely proportional to temperature. This means that, in equations (23) to (25), as T increased, $\frac{n_{H_2}}{V_A}$, $\frac{n_{O_2}}{V_C}$, $\frac{n_{H_2O_C}}{V_C}$ decreased resulting in small time derivatives of $\frac{dPH_2}{dt}$, $\frac{dPO_2}{dt}$, and $\frac{dPH_2O_C}{dt}$, and consequently small changes in the output voltage.

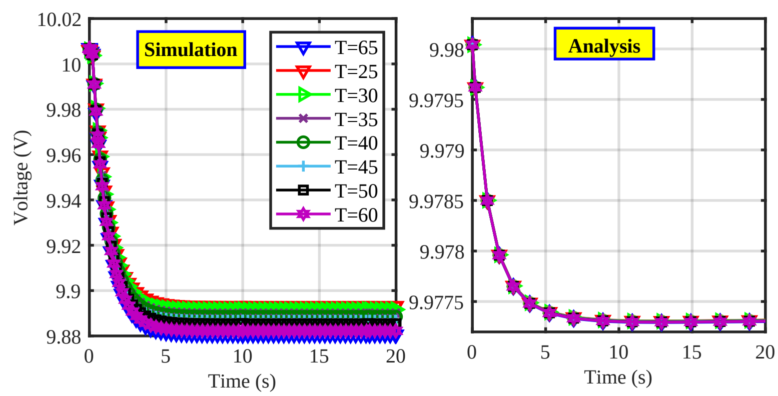

Figure 11: Output voltage (V) of the PEMFC vs. the temperature (in °C).

5.1.5. Voltage as a function of current

This case study investigated the effect of varying current densities on the output voltage of the PEMFC, as depicted in Figure 12. The left subplot shows the time-domain simulation of output voltage vs. input current (current density times the cell's active area), and the right subplot illustrates the output voltage vs. time for various output current values. Since the current is not an input in time-domain simulations, the V-I curve of the PEM fuel cell in time-domain model was used that present the relationship between the voltage at different currents during steady-state operation. The vertical lines in the simulation plot point out voltage values correlated with the current values used for small-signal analysis, with matching colors. According to the equations 16 and 22, regardless of the amount of the current density, the output voltage of PEMFC will drop once the circuit is closed. This was verified in the analysis results in Figure 12, where for each current level, the output voltage dropped at the beginning until it reached a steady-state level. However, once the system reached steady-state, the output voltage in both sets of results was the highest when the current was at the highest level. In the analysis results, the output voltage was obtained as 9.888 and 9.979V corresponding to $I = 10$ and $50A$, respectively. In the simulation results, voltage was measured as 9.99 and $10.05V$ for $I = 10$ and $50A$, respectively. Such 1.1% error between the simulation and analysis results stemmed from the fact that different initial parameters were used in two models as some initial parameters could not be changed in the time-domain simulations. Both the simulation and the analysis results agreed with the Ohm's law, as for any electrical circuit (including fuel cells) voltage is directly proportional to the current for a constant resistance, and thus V increases as I increases: $V = ZI$, where V is the voltage phasor, I is the current phasor, and Z is the impedance of the load which is pure resistive (1.68Ω) in this case.

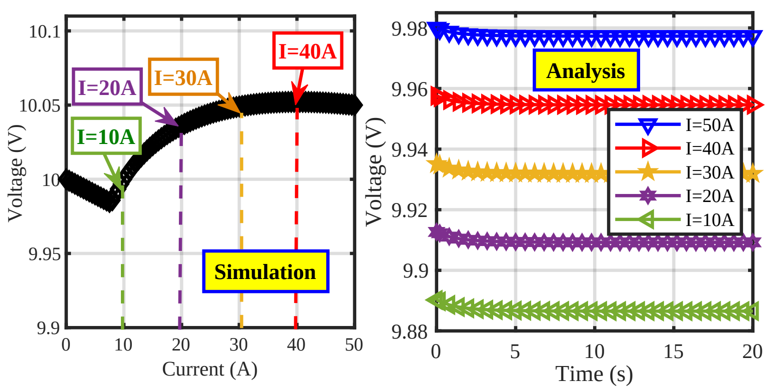

Figure 12: Output voltage (V) of the PEMFC vs. the current (A).

5.1.6. *Voltage as a function of relative humidity in the anode and the cathode*

As stated earlier, the water in the cathode is a more complex variable than that in the anode, which is why it was chosen as one of the state variables. However, the relative humidity in the anode is also important, which is why it was considered as an input variable to the state-space model. In this case study, the dynamic response of the output voltage under variable cathode/anode relative humidity levels was analyzed to identify the values at which the highest voltage was obtained. As seen in the left subplot of Figure 13, the highest and the lowest voltage values were obtained at the cathode relative humidity of 99% and 10%, respectively. At 90% relative humidity in the cathode, the voltage loss was minimized and then completely disappeared as the relative humidity was increased up to 99%. In fact, at this humidity level, the voltage level increased with time, a case that was not observed with any of the other operating variables. In contrast, the anode relative humidity had a small effect on the voltage variations. As exhibited in the right subplot of Figure 13, voltage reached steady-state at a slower pace if relative humidity was below 40%. Once the steady-state was reached, the highest voltage was obtained at 10% anode relative humidity, whereas the lowest voltage happened at the highest anode relative humidity of 99%. This can be explained by the interference of the water molecules in the hydrogen oxidation half-reaction and slowing down the transfer of the released electrons out of the anode, and also the potential flooding that might have occurred at high water concentration [23].

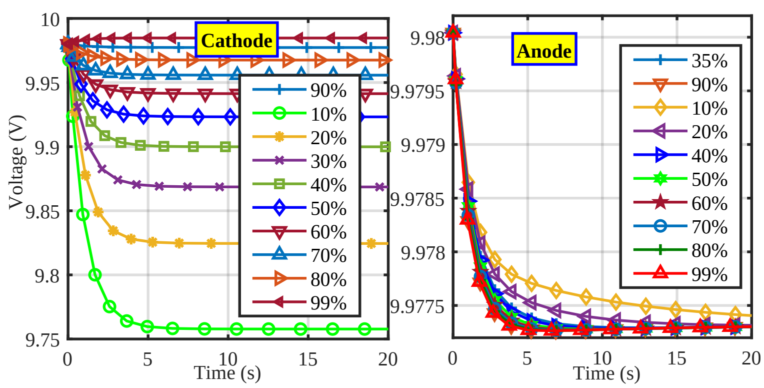

Figure 13: Output voltage of the PEMFC for various relative humidity levels in cathode (left) and anode (right).

5.2. Discussions

The electrochemical state-space model was validated using time-domain simulations for various operating conditions. The results of the small-signal state-space modeling agreed with the simulation results. It should be noted that while the analysis results are obtained from linearized small-signal model, the simulation results were obtained from a time-domain model, which is nonlinear in general. Furthermore, the differences between the initial conditions in the small-signal model and simulated model resulted in slight differences in the outputs. However, as verified in all cases, the trends were similar for the two sets of plots obtained from simulation and analysis, affirming similar correlation between the studied models.

The dynamic behaviour of the voltage followed a logarithmic decay and the output voltage changed as the operating conditions changed. A fuel cell with

more cells may demonstrate a larger voltage drop because the amount of voltage losses were multiplied by the number of the cells, but the overall power was shown to be increased due to the higher current generated by the cells, combined. Higher hydrogen and oxygen flow rates generated higher output voltage values than those at the lower rates. However, because both the fuel and air flow rates were supplied beyond their stoichiometric requirements, the difference in the voltage values of the highest and lowest flow rates was very small. Changing the temperature from 298.15 to $338.15K$ did not make a significant change in the output voltage, which could be explained by the simultaneous decrease occurred in the density of oxygen, hydrogen, and water. The current had two different effects on the voltage; one in the voltage losses and one in the overall generated voltage. The former caused the voltage plummeted immediately after the circuit was closed for the fuel cell to start the operation, while the latter was directly proportional to the current level and its proportional 'ohmic relation' with voltage, in presence of a constant impedance. Even after the current-associated losses are counted into account, a higher current still generated a higher level of voltage in the fuel cell.
Finally, the effect of the cathode water content on voltage was substantial. The higher the water content in the cathode the higher the voltage. However, providing such humidity level could be challenging. The humidity level could be increased by one of the following: lowering the rate of air flow which would reduce cathode performance, increasing the air and fuel pressure which would require energy to run the compressors, or condensing the water from the outlet gas and use it to humidify the inlet air to the cathode which would require extra equipment, weight, size and cost [23]. Thus, it is crucial to find an optimum point at which sufficient humidity is supplied for a reasonable performance which comes also at a justifiable cost and energy.

6. Conclusions

In this paper, a small-signal state-space model was developed for grid-connected PEM fuel cells including the dynamics of fuel cell stack, DC/DC converter, DC/AC converter, LCL filter, and control loops of the converters. The stability analysis for this system indicated a high sensitivity towards changes in DC-link capacitor, boost converter inductance, boost converter controller gains, and PLL gains. Though increasing the DC-link capacitor or inductance values could, respectively, reduce the voltage and current harmonics in the output, it is crucial to be aware of the potential instability that such increase could cause in the overall fuel cell system.
Among various operating parameters in a single PEMFC stack, humidity of the cathode appeared to be the most influential element on the output voltage of the fuel cell stack, demonstrating the highest voltage at 99% cathode humidity. When the inlet air flow rate was below 1 Lpm, the output voltage dropped. However, increasing inlet air flow at rates higher than 5 Lpm did not increase, nor did it decrease the output voltage of the PEMFC. Based on the acquired

results, this work proposes the following optimum conditions for a 100W polymer electrolyte membrane fuel cell: $N = 20$ cells, fuel flow rate = 2.0 Lpm, air flow rate = 11 Lpm, $T = 50°\text{C}$, $I = 50A$, cathode relative humidity = 99%, and anode relative humidity = 40%. Due to the high cost and complexity incurred as a result of providing 99% humidity, it is recommended to use 60% cathode humidity, at which the output voltage would be only slightly lower (0.03V) but achievable with most fuel cell humidifiers available in the market. These results will be used in the next step of this study which will be focused on 1) developing ”optimal” controller and PLL gains, 2) analyzing ”time-domain” of the proposed framework, and 3) ”experimental” validation of the developed model on a lab-scale microgrid.

7. Funding

This research did not receive any specific grant from funding agencies in the public, commercial, or not-for-profit sectors.

References

[1] James Larminie, Andrew Dicks, and Maurice S McDonald. *Fuel cell systems explained*, volume 2. J. Wiley Chichester, UK, 2003.

[2] Dennis E Curtin, Robert D Lousenberg, Timothy J Henry, Paul C Tangeman, and Monica E Tisack. Advanced materials for improved PEMFC performance and life. *Journal of Power Sources*, 131(1-2):41–48, 2004.

[3] Jeffrey Fergus, Rob Hui, Xianguo Li, David P Wilkinson, and Jiujun Zhang. *Solid oxide fuel cells: materials properties and performance*. CRC press, 2016.

[4] Leo JMJ Blomen and Michael N Mugerwa. *Fuel cell systems*. Springer Science & Business Media, 2013.

[5] A John Appleby. Fuel cell handbook. 1988.

[6] Frano Barbir. *PEM fuel cells: theory and practice*. Academic Press, 2012.

[7] Xing Luo, Jihong Wang, Mark Dooner, and Jonathan Clarke. Overview of current development in electrical energy storage technologies and the application potential in power system operation. *Applied Energy*, 137:511–536, 2015.

[8] Samuel Simon Araya, Fan Zhou, Vincenzo Liso, Simon Lennart Sahlin, Jakob Rabjerg Vang, Sobi Thomas, Xin Gao, Christian Jeppesen, and Søren Knudsen Kær. A comprehensive review of PBI-based high temperature PEM fuel cells. *International Journal of Hydrogen Energy*, 41(46): 21310–21344, 2016.

[9] Jenn-Kun Kuo and Chi-Fa Wang. An integrated simulation model for PEM fuel cell power systems with a buck DC–DC converter. *international journal of hydrogen energy*, 36(18):11846–11855, 2011.

[10] Lu-Ying Chiu and Bill M Diong. An improved small-signal model of the dynamic behavior of PEM fuel cells. In *38th IAS Annual Meeting on Conference Record of the Industry Applications Conference, 2003.*, volume 2, pages 709–715. IEEE, 2003.

[11] K Latha, S Vidhya, B Umamaheswari, N Rajalakshmi, and KS Dhathathreyan. Tuning of PEM fuel cell model parameters for prediction of steady state and dynamic performance under various operating conditions. *International Journal of Hydrogen Energy*, 38(5):2370–2386, 2013.

[12] Tolga Taner. Energy and exergy analyze of PEM fuel cell: a case study of modeling and simulations. *Energy*, 143:284–294, 2018.

[13] Im Mo Kong, Aeri Jung, and Min Soo Kim. Investigations on the double gas diffusion backing layer for performance improvement of self-humidified proton exchange membrane fuel cells. *Applied Energy*, 176:149–156, 2016.

[14] Bosung Kim, Dowon Cha, and Yongchan Kim. The effects of air stoichiometry and air excess ratio on the transient response of a PEMFC under load change conditions. *Applied Energy*, 138:143–149, 2015.

[15] Alessandra Perna, Mariagiovanna Minutillo, and Elio Jannelli. Investigations on an advanced power system based on a high temperature polymer electrolyte membrane fuel cell and an organic rankine cycle for heating and power production. *Energy*, 88:874–884, 2015.

[16] Y Bicer, I Dincer, and M Aydin. Maximizing performance of fuel cell using artificial neural network approach for smart grid applications. *Energy*, 116: 1205–1217, 2016.

[17] ID Gimba, AS Abdulkareem, A Jimoh, and AS Afolabi. Theoretical energy and exergy analyses of proton exchange membrane fuel cell by computer simulation. *Journal of Applied Chemistry*, 2016, 2016.

[18] Shang-Wen Tsai and Yong-Song Chen. A mathematical model to study the energy efficiency of a proton exchange membrane fuel cell with a dead-ended anode. *Applied Energy*, 188:151–159, 2017.

[19] Adam Z Weber and John Newman. Modeling transport in polymer-electrolyte fuel cells. *Chemical Reviews*, 104(10):4679–4726, 2004.

[20] Caisheng Wang, MH Nehrir, and Hongwei Gao. Control of PEM fuel cell distributed generation systems. *IEEE Transactions on Energy Conversion*, 21(2):586–595, 2006.

[21] JM Andujar, F Segura, and MJ Vasallo. A suitable model plant for control of the set fuel cell- DC/DC converter. *Renewable Energy*, 33(4):813–826, 2008.

[22] Ya-Xiong Wang and Young-Bae Kim. Real-time control for air excess ratio of a PEM fuel cell system. *IEEE/ASME Transactions on Mechatronics*, 19 (3):852–861, 2014.

[23] Andrew Dicks and David Anthony James Rand. *Fuel cell systems explained*. Wiley Online Library, 2018.

[24] Lu-Ying Chiu, Bill Diong, and Randall S Gemmen. An improved small-signal model of the dynamic behavior of PEM fuel cells. *IEEE Transactions on Industry Applications*, 40(4):970–977, 2004.

[25] Sandip Pasricha and Steven R Shaw. A dynamic PEM fuel cell model. *IEEE Transactions on Energy Conversion*, 21(2):484–490, 2006.

[26] PJH Wingelaar, JL Duarte, and MAM Hendrix. PEM fuel cell model representing steady-state, small-signal and large-signal characteristics. *Journal of Power Sources*, 171(2):754–762, 2007.

[27] Bei Gou, Woonki Na, and Bill Diong. *Fuel cells: modeling, control, and applications*. CRC press, 2009.

[28] Vahid Samavatian and Ahmad Radan. A high efficiency input/output magnetically coupled interleaved buck–boost converter with low internal oscillation for fuel-cell applications: Small signal modeling and dynamic analysis. *International Journal of Electrical Power & Energy Systems*, 67:261–271, 2015.

[29] Vasudha Khubchandani, Kamlesh Pandey, Vijay Kumar Tayal, and Sanjay Kumar Sinha. PEM fuel cell integration with using fuzzy PID technique. In *2016 IEEE 1st International Conference on Power Electronics, Intelligent Control and Energy Systems (ICPEICES)*, pages 1–4. IEEE, 2016.

[30] Amirnaser Yazdani and Reza Iravani. *Voltage-sourced converters in power systems*, volume 34. Wiley Online Library, 2010.

[31] Mohan, Ned and Undeland, Tore M. *Power electronics: converters, applications, and design*. John Wiley & Sons, 2007.

[32] Bacha, Seddik and Munteanu, Iulian and Bratcu, and Antoneta Iuliana. Power electronic converters modeling and control. *Advanced Textbooks in Control and Signal Processing*, 454:454, 2014.

[33] P. L. Dandeno and P. Kundur. Practical application of eigenvalue techniques in the analysis of power system dynamic stability problems. *Canadian Electrical Engineering Journal*, 1(1):35–46, Jan 1976. ISSN 0700-9216. doi: 10.1109/CEEJ.1976.6830824.

[34] Werner Stumm and James J Morgan. *Aquatic chemistry: chemical equilibria and rates in natural waters*, volume 126. John Wiley & Sons, 2012.

[35] Farhani Slah, Amari Mansour, Marzougui Hajer, Bacha Faouzi, et al. Analysis, modeling and implementation of an interleaved boost DC-DC converter for fuel cell used in electric vehicle. *International Journal of Hydrogen Energy*, 42(48):28852–28864, 2017.

[36] Mark M Benjamin. *Water chemistry*. Waveland Press, 2014.

[37] J Mahdavi, A Emaadi, MD Bellar, and M Ehsani. Analysis of power electronic converters using the generalized state-space averaging approach. *IEEE Transactions on Circuits and Systems I: Fundamental Theory and Applications*, 44(8):767–770, 1997.

[38] J. Khazaei, D. H. Nguyen, A. Asrari, and H. A. Mohammadpour. Small-signal stability evaluation of DFIG wind farms with on-site battery energy storage. In *2019 IEEE PES GTD Grand International Conference and Exposition Asia (GTD Asia)*, pages 274–279, March 2019. doi: 10.1109/GTDAsia.2019.8715961.

[39] Khazaei, Javad and Miao, Zhixin and Piyasinghe, Lakshan. Impedance-model-based MIMO analysis of power synchronization control. *Electric Power Systems Research*, 154:341–351, 2018.

[40] Khazaei, Javad and Beza, Mebtu and Bongiorno, Massimo. Impedance analysis of modular multi-level converters connected to weak AC grids. *IEEE Transactions on Power Systems*, 33(4):4015–4025, 2017.

[41] Emilio Figueres, Gabriel Garcerá, JesÚs Sandia, Francisco Gonzalez-Espin, and JesÚs Calvo Rubio. Sensitivity study of the dynamics of three-phase photovoltaic inverters with an LCL grid filter. *IEEE Transactions on Industrial Electronics*, 56(3):706–717, 2009.

[42] Joseph F Zemaitis Jr, Diane M Clark, Marshall Rafal, and Noel C Scrivner. *Handbook of aqueous electrolyte thermodynamics: theory & application*. John Wiley & Sons, 2010.